Silanization of 3D-Printed Silica Fibers and Monoliths

Peer-reviewed author version

Vogelsang, David; ADRIAENSENS, Peter; Wyns, Kenny; Michielsen, Bart; Gys, Nick & Mullens, Steven (2022) Silanization of 3D-Printed Silica Fibers and Monoliths. In: ACS Applied Materials & Interfaces, 14 (25) , p. 29345 -29356.

DOI: 10.1021/acsami.2c03844
Handle: http://hdl.handle.net/1942/37799

Silanization of 3D-printed silica fibers and monoliths

David Vogelsang[1], Peter Adriaensens[2], Kenny Wyns[1], Bart Michielsen[1], Nick Gys[1,3], Steven Mullens[1]*

[1]VITO, Unit Sustainable Materials, Boeretang 200, BE-2400 Mol, Belgium

[2]Applied and Analytical Chemistry, Institute for Materials Research, Hasselt University, Agoralaan 1 Building D, 3590 Diepenbeek, Belgium

[3]Laboratory of Adsorption and Catalysis, Department of Chemistry, University of Antwerp, Universiteitsplein 1, 2610 Wilrijk, Belgium.

ORCID

David Vogelsang: 0000-0002-6564-7046

Peter Adriaensens: 0000-0003-4183-0150

Kenny Wyns: 0000-0003-4208-3038

Bart Michielsen: 0000-0003-1720-4037

Nick Gys: 0000-0003-1464-6331

Steven Mullens: 000-0002-2614-151X

Contact Author

*David Vogelsang – david.vogelsang@vito.be

Abstract

Surface functionalization of complex 3-dimensional porous architectures has not been widely investigated despite their potential in different application domains. In this work, silanization was performed in silica 3D-printed porous structures, and the homogeneity of functional groups

within the architecture investigated by comparing the extent of the functionalization in the walls and core of the monolith. A silica ink was used for direct ink writing (DIW) to shape fibers and monoliths with different architectures and stacking designs. The surfaces of the fibers and monoliths were functionalized with 3-aminopropyl(triethoxysilane) (APTES) using different reaction conditions. The nature of the functional groups on the surface, and the presence of $RSiO_{1.5}$ bonds, were identified by solid state ^{13}C-NMR, ^{29}Si-NMR and by ξ-potential measurements. Elemental analysis was used to quantify the concentration of bonded APTES in the core and walls of the monolith. The availability and hydrolytic stability of the introduced amine group on fibers was evaluated using the adsorption of $PdCl_4^{2-}$ ions within the pH range of 2 to 5. The study found that geometries with interfiber distances above 250 μm are homogeneously functionalized with amine groups. As interfiber distance of the monolith decreases, a significantly lower density of amine groups is detected in the core of the monolith. The determination of the homogeneity of 3D-printed monoliths makes this work relevant as it provides the limits of functionalization carried out in stirred batch reactors for geometrically defined structures produced from a 3D-printing process.

Keywords: silanization, direct ink writing, 3D-printing, silica, APTES, gap-spanning structures, Pd sorption

1. Introduction

Silanization of silica surfaces has been widely described in literature and has been applied in diverse applications such as catalysis, chromatography, and adsorption processes.[1–7] In particular, adsorption of organic compounds like proteins and polymers, and metals such as palladium (Pd) has been reported for silica functionalized with mercaptopropyl and aminopropyl groups.[8–10] The reaction between the surface and alkoxysilanes can be performed using diverse protocols including vapor deposition, dipping, perfusion, or in solution with stirred batch reactors.[11–13]

Silanization of silica powders and spheres have been extensively reported. One of the most common silanization protocols for particles is the functionalization in solution inside stirred batch reactors.[14–16] It is accepted that the silanization occurs homogeneously, understood as a constant density of functional groups throughout the sample, because the silica surface is uniformly exposed to the silanes in solution. Silanization has also been reported for macroscopic silica materials with complex porous architectures such as sol-gel casted structures, capillaries, and more recently 3D-printed monolithic structures manufactured by Direct Ink Writing (DIW).[11,17–22]

The densities of functional groups in silanized macroscopic silica structures have been reported as a constant value by multiple authors.[17,23,24] Therefore, it has been assumed that the functionalization is homogeneous throughout the structure. Currently, the only report describing silanization of silica gap-spanning structures manufactured by DIW is Thakkar *et al* using aminopropyl(triethoxysilane) (APTES), this research reported similar content of nitrogen in functionalized powders than the nitrogen content in the monolith.[17] However, the architecture of the monoliths composed by the fiber diameter, the interfiber distance, and the stacking of each printed layer may have an effect in the extent of functionalization and in the

homogeneity of the functional groups density within the monolith. Functionalization homogeneity within the fibers and throughout the monolith could have a direct implication in adsorption processes as higher adsorption capacities could be reached if the surface is fully covered.[25] Therefore, to completely understand the potential and limitations of batch functionalization, the geometry and the infill characteristics of the materials manufactured by DIW should be linked with different functionalization conditions. Current state of the art in DIW of silica can be divided between the manufacturing of dense and porous silica structures. Dense structures have been mainly manufactured for optical applications utilizing silica microspheres,[26] glass powder,[27,28] and sol-gel feedstocks.[29] On the other hand, studies involving DIW of porous silica structures used powder based,[17,30,31] and template assisted sol-gel systems.[32]

The main goal of this work was to assess the homogeneity of the silanization in 3D-printed gap-spanning structures with porous fibers and controlled channeling using a stirred batch reactor. Variations in temperatures, reaction times, and concentrations of silane were used to evaluate the effect of the reaction parameters on the homogeneity of functional groups in the monoliths. To achieve this goal, an ink formulation based on powder and colloidal silica was developed and characterized. Fibers and monoliths were shaped by DIW and characterized by nitrogen sorption, scanning electron microscopy (SEM), and thermogravimetry (TGA). The fibers and monoliths were then silanized with APTES using variations in temperature, reaction time, and concentration in a stirred batch reactor. The occurrence of mass transfer limitations to the interior of the monolith, or within the pore structure of the fibers itself, are investigated using the comparison of the extent of functionalization of ground monoliths. **Scheme 1** illustrates the workflow proposed in this research. This information is used to make practical decisions regarding the functionalization procedures for 3D-printed structures.

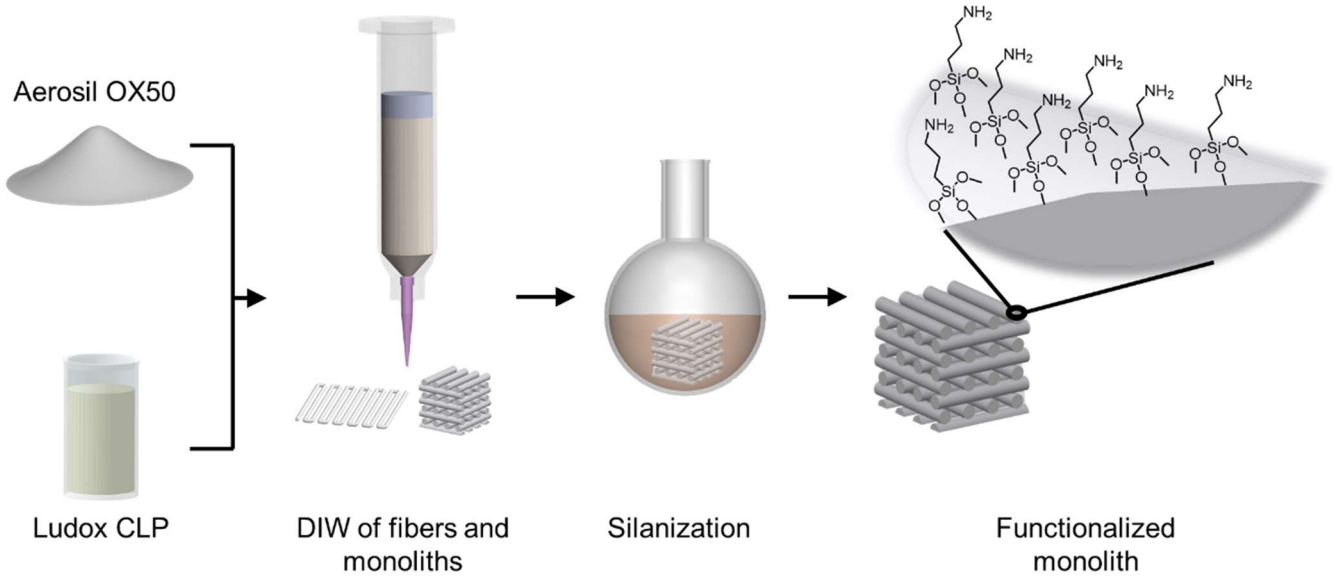

Scheme 1. Workflow proposed in this manuscript including mixing, printing, and silanization of the structures with APTES.

2. Experimental

2.1. Materials

Preparation of the ink was made with Aerosil® OX-50 (OX50) with particle sizes between 50 nm and 80 nm supplied by Evonik, LUDOX® CL-P (CLP) with particles of 22 nm donated by Grace, and lanolin purchased from Fagron. The silanization reagent APTES was acquired from sigma, while toluene, triethylamine (TEA), and 4 Å molecular sieves were purchased from VWR. In addition, the toluene was dried with the molecular sieves before the experiment started. Furthermore, the silicone/polyethylene (PE) coated paper was supplied by Aubry Papier. If not stated in the text, all materials and reagents were used as received.

2.2. Silica ink preparation

The ink for DIW was formulated by mixing CLP and OX50 as solids sources, and lanolin as rheology and a drying agent. A standard formulation was prepared by adding 8.9 g of lanolin,

50 g of CLP, and 41 g of OX50 in a container suitable for mixing in the planetary mixer SpeedMixer DAC 1400-1000 VAC. The OX50 was added in multiple steps and in every step mixed for two minutes until a total of 41 g were reached.

2.3. 3D-printing of fibers and monoliths

The ink was transferred to a syringe barrel and extruded through conical nozzles. Occasional nozzle blockage, due to the presence of powder agglomerates, was observed with nozzle diameters below 400 µm. Sieving the ink through a mesh of 30 µm using a reusable syringe filter assembly avoided the clogging and resulted in a continuous extrusion. The syringe was installed in a n-Scrypt 3Dn-500 3D-printer, conditioned at 20 °C with a relative humidity between 45% and 55%. All the structures were extruded on top of the PE side of the silicone/PE coated paper. Fibers were extruded continuously using different nozzle diameters of 200 µm, 400 µm, 600 µm, 800 µm, 1100 µm and 1600 µm. Monoliths were printed using either 200 µm or 400 µm nozzles, with two types of stacking designs. Gap-spanning structures were printed as grids to achieve simple cubic structures (SC) and face-centered cubic structures (FCC)[33]. Reference images for the SC and FCC internal configurations are shown in **Figure S1**.

The interfiber distance (IFD) was varied between 150 µm and 250 µm and 1 cm cubes were printed using the configurations described in **Table 1**. The supplemental movie shows the printing of a structure utilizing the formulated ink. After printing, the structures were dried at an average temperature of 20 °C and relative humidity between 45% and 55%. Drying times were approximately 2 hours for the structures with larger gaps, and 48 hours for the finest patterns, No cracking was observed after drying. Next, the structures were removed from the surface of the PE coated paper and placed on top of an alumina plate. The samples were then thermally treated by heating at 60 °C/h to reach 600 °C inside a chamber furnace Nabertherm

LH 30/14. The temperature of the furnace was maintained at 600 °C for 4 h before cooling down to room temperature. In addition, thermally treated structures were ground and used as a control sample for the functionalization experiments. The ground monoliths (GM) had a d_{50} particle size of 16 µm (**Figure S2**).

Table 1. Description of the infill details including interfiber distance (IFD), fiber diameter (FD), and type of stacking used between simple cubic structures (SC), and face-centered cubic structures (FCC).

Sample ID	Nozzle diameter (µm)	IFD set (µm)	Stacking	FD after thermal treatment (µm)	IFD after thermal treatment (µm)
200/250-SC	200	250	SC	206 ± 18	241 ± 14
400/250-SC	400	250	SC	354 ± 20	253 ± 15
200/150-SC	200	150	SC	213 ± 18	141 ± 15
200/150-FCC	200	150	FCC	194 ± 12	153 ± 19

2.4. Silanization of 3D-printed fibers and ground monoliths

Silanization with aminopropyl-alkoxysilanes has been researched because its use in diverse applications,[7,14,34,35] the particularity of the chain bending towards the surface,[11,36,37] and as it is a self-catalytic reaction that can be performed in gas phase or in liquid phase.[15,38] In this work, silanization of 3D-printed fibers and GM was performed in solution in a batch stirred reactor. All samples and glassware were stored at 75 °C prior to silanization. The solids were functionalized by silanization based on a protocol described in the literature.[36] APTES and

TEA were added into a container, mixed under a nitrogen stream and a 60 mL syringe filled with the resulting reaction mixture. Simultaneously, known masses of 3D-printed silica fibers and GM were placed separately in a two neck round bottom flask. A vacuum line with a valve was attached to one of the necks and the flask sealed by a rubber septum on the other neck. Vacuum was induced into the flask for 3 to 5 minutes before closing the valve. The rubber septum in the two-neck flask was penetrated with the syringe containing the reaction mixture that was sucked into the flask by the vacuum and resulted in the immediate impregnation of the material. The vacuum line was removed from the flask to be replaced by a condenser. Afterwards, the solution with the solids was stirred at 50 rpm for 2 h or for 24 h. The samples were filtered using 0.25 μm cellulose fiber filters, flushed with nitrogen, and washed three times sequentially with acetone, water, and acetone. After washing the samples were flushed with a nitrogen stream, dried at 75 °C for 24 h, and stored in closed vials in an oven at 75 °C to limit water adsorption by the surface.

2.5. Silanization kinetics of 3D-printed monoliths

The kinetics of the silanization reaction were investigated on silica monoliths with the configuration 200/150-SC. The monoliths were vacuum impregnated using a 20 mM solution of APTES in toluene and TEA (3:1 ratio for each mol of APTES) and reacted over time under reflux conditions. The structures were reacted using time intervals ranging from 0.5 h to 24 h in a round bottom flask that performed the function of a batch reactor. The samples were washed with acetone, followed by a washing/hydrolysis step using water and washed again using acetone. All washing steps were done using vacuum impregnation processes. The washing was followed by drying the structures in an oven at 60 °C for 24 h.

2.6. Extent of silanization and homogeneity in 3D-printed structures

Two silanization protocols were applied to assess the extent and the homogeneity of the functionalization between the wall and the core of the monoliths. All samples and glassware were stored at 75 °C prior to being used in the silanization. In the first procedure, the reactions were maintained at room temperature, under reflux with dry toluene as solvent, APTES as reagent, and TEA as the reaction promotor. The stoichiometry was based on a theoretical hydroxyl density of 2.1 #OH/nm^2.[39] The experiment involved adding toluene, APTES, and TEA (a 1:3 ratio of APTES:TEA) into a round bottom flask. Silanol:APTES ratios equal to 1.1:1 or 1:7, depending on the treatment, were used in the mixtures. The solution was mixed under a nitrogen stream and the reaction mixture placed inside a 60 mL syringe. Next, a known mass of 3D-printed monolith was placed into a two neck round bottom flask. A vacuum line with a valve was attached to one of the necks and the flask sealed by a rubber septum on the other neck. A vacuum (minimum pressure = 100 mbar) was induced into the flask for 3 to 5 minutes before the valve was closed. The rubber septum in the two-neck flask was penetrated with the syringe containing the reaction mixture that was then sucked into the flask, resulting in the immediate impregnation of the monolith. The vacuum line was removed from the flask to be replaced by a condenser. The functionalization conditions are listed in **Table 2**. The samples were taken out of the solution, flushed with nitrogen, washed three times sequentially with acetone, water, and acetone. The samples were dried by flushing with a nitrogen stream, and further treated at 75 °C for 24 h. The cores and the walls of the monoliths were cut as pictured in **Figure S3** using a diamond blade of 500 µm rotating at 2000 rpm without water, while moving the sample at a speed of 0.02 mm/s.

A second procedure adapted from Krasnoslobodtsev and Smirnov was developed to increase the extent of functionalization at the surface of the monoliths, and to reduce the

reaction time.[38] This procedure was performed using multiple vacuum wetting by forcing fresh APTES into the unreacted pores. In this procedure, monoliths of 400/250-SC cubic-like shape and a silanol:APTES ratio equal to 1.1:1 (APTES 2.5 mM concentration) were maintained at room temperature for 0.5 h. The samples were washed after synthesis using vacuum impregnation washing processes first with acetone, followed by a washing/hydrolysis step using water, and a second washing with acetone. The samples were then dried in an oven at 80 °C for 30 min and the reaction and washing steps repeated two more times. This treatment was labeled as 2.5-0.5-RT-X3. All the reaction experiments were performed in duplicate.

Table 2. Experimental conditions for APTES functionalization of silica monoliths.

Silanization code	Concentration (mM)	Time (h)	Temperature (°C)
20-0.5-RT	20	0.5	20
20-0.5-Ref	20	0.5	110
20-24-RT	20	24	20
20-24-Ref	20	24	110
2.5-0.5-RT	2.5	0.5	20
2.5-0.5-Ref	2.5	0.5	110
2.5-24-RT	2.5	24	20
2.5-24-Ref	2.5	24	110

2.7. Pd adsorption experiments

The availability of the amine groups to interact with the environment was verified by performing Pd adsorption experiments, using untreated fibers and fibers functionalized with APTES. The influence of pH in the adsorption of Pd was studied at pH 2.0 ± 0.1, 3.0 ± 0.1, 4.0 ± 0.1, and 5.0 ± 0.1. Since the Pd speciation strongly depends on the pH of the solution and the chloride concentration, a solution of Pd with a concentration of 150 mg/L at pH 1 was prepared by dissolving palladium dichloride ($PdCl_2$, Sigma Aldrich) in hydrochloric acid (HCl) for 24 h to ensure a fixed concentration of chlorine (Cl). Stock solutions of Pd adjusted to pH 2, 3, 4, and 5 were prepared with sodium hydroxide (NaOH) solutions to determine the maximum adsorption capacity for Pd adsorption. For each adsorption experiment, 200 mg of fibers were placed in a sample holder with a bottom polyethylene mesh (350 µm, PVF GmbH) to avoid mechanical damage to the fibers. The sample holder was inserted into a plastic vial, 20 ml of the Pd solution was added, and the system was stirred at 300 rpm for 24 hours with a magnetic stirrer located between the plastic vial and the sample holder. All experiments were performed in duplicate. The Pd and silicium (Si) concentrations in the starting solutions, as well as in the solutions after adsorption, were measured by inductively coupled plasma optical emission spectroscopy (ICP-OES, Agilent Technologies 5100). The adsorption capacity (Q_e) is calculated from **Equation 1** where m_e is the mass of adsorbant (g), C_o is the initial concentration of the metal in the solution in mg/L, C_e is the concentration of the metal in equilibrium in mg/L, and V is the volume of solution in L.

Equation 1

$$Q_e = \frac{C_o - C_e}{m_e} V$$

2.8. Characterization

Rheological characterization of the ink was made in a Thermo Haake MARS 60 instrument with 3.5 cm diameter parallel plates for oscillatory experiments, and with 3.5 cm and 2° angle cone and plate for the steady state experiments. For oscillatory experiments, the measurements were made by conditioning the ink for 10 minutes at a shear stress of 0.001 Pa using 2% strain, followed by a shear stress swap between 0.001 Pa and 1000 Pa with 2% strain. Steady state experiments were performed by conditioning the sample for 5 minutes with a shear rate of 0.01 s^{-1}. The shear rate was varied between 0.001 s^{-1} and 100 s^{-1}.

Solid contents of the inks were obtained by placing a known mass of the ink on a heating plate and heating at 60 °C/h to reach 600 °C in a Nabertherm LH 30/14 chamber furnace. The temperature was then maintained for 4 h before cooling down to room temperature. The weight was measured, and a second thermal treatment was done to verify the final weight. Determination of the interconnectivity of the pores was performed by Hg intrusion porosimetry using a PASCAL 140/240 porosimeter. Pore diameter and pore volume were calculated by BJH from nitrogen sorption isotherms, after degassing the samples at 100 °C and 0.01 mbar, measured in an autosorb iQ2 MP instrument (Quantachrome GmbH). Furthermore, the specific surface area (SSA) was calculated by the Brunauer–Emmett–Teller (BET) model. Hydroxyl quantification was performed based on the work of Mueller *et al*[39] that used the SSA and the weight loss calculated from TGA using a NETZSCH STA 449C instrument. For TGA, the sample was heated in a nitrogen atmosphere (70 mL/min) from 25 °C to 120 °C at 10 °C/min, then held at 120 °C for 10 min, and followed by a heating ramp from 120 °C to 800 °C at 20 °C/min. In the final step, the sample was maintained at a temperature of 800 °C for 10 min.

The structure homogeneity and the infill patterns of the printed structures were examined by optical microscopy. In order to do so, the fiber diameter (FD) and the IFD were measured

in different sections of each monolith. Reported values were collected from the cross section of the monolith and are based on more than 50 measurements in the top, middle, and bottom positions. The images were acquired using a Zeiss Discovery V12 stereomicroscope, equipped with a Plan Apo S 1.0xFWD 60 mm objective and image collection performed using an Axiovision MRc digital camera connected to the microscope. SEM-EDS images were acquired using a Nova Nano SEM 450 (FEI, USA) cold field emission scanning electron microscope (FEGSEM) operating at an acceleration voltage of 5 kV. Quantification of carbon and nitrogen in the samples was made by elemental analysis using a Elementar vario EL cube. ξ-potential measurements were performed for cores and walls of the sample 200/150-SC and 400/250-SC, using the treatment 20-24-Ref, as well as a control sample without functionalization in the surface that serves as a reference. The ξ-potentials were identified on a ZetaSizer Nano ZS instrument (Malvern Panalytical) by grinding the monoliths and suspending 20 mg of the ground powder in 10 mL of a 10 mM potassium chloride (KCl) solution. The suspension was divided into aliquots and the pH of each aliquot adjusted to more basic or acid pH using 0.01 M, 0.1 M and 1 M solutions of NaOH or HCl and the isoelectric points (IEP) were calculated by interpolation.

Formation of bonds between the silica surface of the monoliths and the APTES molecules was followed by solid state NMR using the walls of the samples after cutting as seen in **Figure S3**. Solid-state ^{13}C-CPMAS (Cross-Polarization Magic Angle Spinning) NMR spectra were acquired on a Bruker 400 MHz spectrometer (9.4 Tesla) equipped with a 4 mm probe and magic angle spinning performed at 7 kHz using ceramic zirconia rotors. Furthermore, the aromatic signal of hexamethylbenzene was used to calibrate the carbon chemical shift scale (132.1 ppm). The acquisition parameters used were: a spectral width of 50 kHz, a 90° pulse length of 3.5 μs, an acquisition time of 20 ms, a recycle delay time of 3 s, a spin-lock field of

50 kHz, a contact time of 1 ms, and 75000 accumulations. During acquisition, the high-power proton dipolar decoupling was set to 70 kHz.

Solid-state ^{29}Si-CPMAS NMR spectra were acquired on an Agilent VNMRS DirectDrive 400 MHz spectrometer (9.4 Tesla) equipped with a T3HX 3.2 mm probe and magic angle spinning performed at 6.5 kHz using ceramic zirconia rotors. The talc signal was used to calibrate the silicon chemical shift scale (-98 ppm). Acquisition parameters used were: a spectral width of 24 kHz, a 90° pulse length of 3.2 μs, an acquisition time of 15 ms, a recycle delay time of 5 s, a spin-lock field of 80 kHz, a contact time of 2 ms, and 75000 accumulations. High power proton dipolar decoupling during the acquisition time was set to 80 kHz.

Solid-state ^{1}H-MAS homonuclear dipolar decoupled NMR spectra were acquired on a Jeol ECZ600R 600 MHz spectrometer (14.1 Tesla wide bore magnet) equipped with a 3.2 mm wide VT Range HXMAS probe. Magic angle spinning was performed at 19.5 kHz and proton-proton homonuclear dipolar decoupling performed using a wPMLG-5 pulse sequence. Glycine was used to calibrate the proton chemical shift scale and the peaks set at 3.4 ppm and 4.4 ppm (CH_2 protons), and 8.5 ppm (NH_2). The acquisition parameters used were a spectral width of 55 kHz, a 90° pulse length of 2.3 μs, an acquisition time of 20 ms, a recycle delay time of 20 s, and 32 accumulations.

3. Results and discussion

3.1. Characterization of silica ink for direct ink writing

The printability of the silica ink to manufacture monoliths with different configurations was correlated from viscoelastic and flow experiments after preparation of the ink. A major attribute of the mixed ink is the formulation using silicas with two defined particle sizes that enable printing below the pressure limit of the printer (100 psi) while maintaining a solid

content of 64 %.[40] The viscoelastic behavior of the ink is displayed in **Figure 1a**. The elastic modulus (G') of the ink is 10000 Pa higher than the viscous modulus (G'') within the linear viscoelastic region, indicative of a solid-like behavior when low shear stress is applied. Also, in **Figure 1a** the crossing between G' and G'' occurs at a shear stress (τ_f) value of 900 Pa. As a result, once the ink is extruded, the formed fibers retain their shape, even when stacked into several layers. Furthermore, based on the rheology data shown in **Figure S4** intensive mixing was required to achieve homogeneous inks. The ratio between the value of G' in the linear viscoelastic region and τ_f, known as the Feilden's figure of merit (Φ), was 22.5 which is higher than the printability limit of 20.[41,42] In addition, the steady state graph in **Figure 1b** shows an increase of the shear stress as the shear rate increases. This behavior is typical of non-Newtonian fluids and is beneficial for printability as the viscosity is reduced in function of the shear stress, further demonstrating that this ink is suitable for DIW.

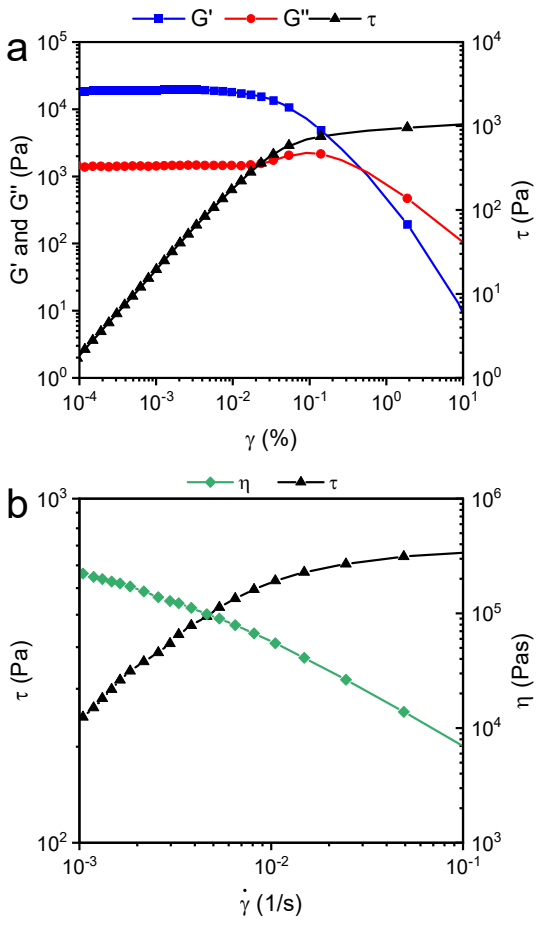

Figure 1. Evolution of the elastic modulus (G'), the viscous modulus (G'') and the shear stress (τ) in function of the imposed strain (γ) to evaluate the viscoelastic behavior of the ink (a), and evolution of the dynamic viscosity (η) and τ in function of the shear rate, showing the shear thinning behavior of the ink (b).

3.2. Printing and printed structures

The printable ink was used to print fibers and monoliths that could be further functionalized. The diameters of these fibers after thermal treatment were 172 ± 3 µm, 356 ± 3 µm, 505 ± 1 µm, 747 ± 4 µm, 1028 ± 3 µm, and 1403 ± 3 µm. Optical microscopy images of the fibers are shown in **Figure S5**. **Figure 2a** and **Figure 2b** show the images from optical microscopy of the top surface of the monolith, demonstrating that printing of monoliths is possible for IFD higher than 150 µm for the 200 µm nozzle, and higher than 250 µm for the 400 µm nozzle. Further decreasing the IFD resulted in merging of the fiber extrudate with the adjacent fibers thereby closing the openings of the monolith (**Figure S1**). FD and IFD are almost identical along the structure as seen in **Figure S6** and **Figure S7**. The average FD and IFD measured from OM images is reported in **Table 1.** Therefore, the monoliths are regarded as homogeneous and they have reproducible porous architectures.

Microstructural analysis of the surface of the silica monoliths reveals a bimodal distribution of sphere-like particles as observed by SEM and shown in **Figure 2c** and **Figure S8**. Smaller spheres of about 22 nm correspond to the size reported by the manufacturer for colloidal silica, while larger spheres between 50 nm and 80 nm match with the reported value for the fumed silica used in this work. It is important to note that no agglomerates of fumed silica were seen, which is indicative of the correct mixing and homogeneity of the ink. The pore size distribution measured by Hg intrusion (**Figure S10)** and calculated by BJH from

nitrogen sorption measurements (**Figure S9)** demonstrate that the structures are mainly mesoporous.

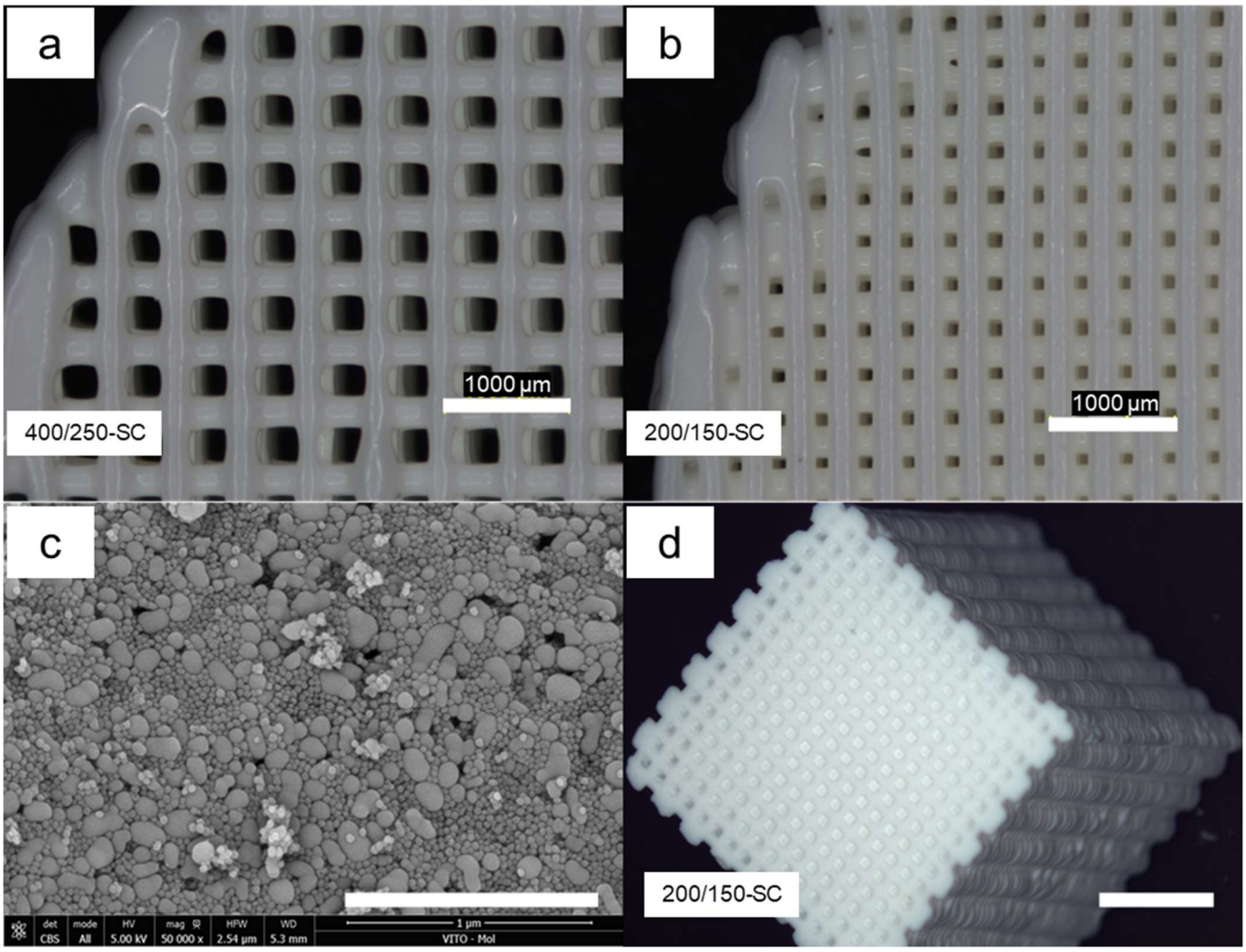

Figure 2. Optical microscopy of the top surface of a 400/250-SC monolith (**a**) and a 200/150-SC monolith (**b**); SEM image of the monolith surface showing a bimodal distribution between colloidal and fumed silica (**c**); cubic structure used in the functionalization experiments (**d**). Scalebars represent 1 µm, for **c**; and 3 mm for **d**.

3.3. Functionalization of silica ground monoliths and fibers

Ensuring a full access of APTES within the interior of each extruded fiber is required to reach full functionalization. The approach followed in this work consisted in the silanization

of GM and extruded silica fibers (ESF) and comparing the extent of their functionalization thereby avoiding the complexities of 3D-printed geometries. GM and ESF were functionalized with APTES using the first reaction procedure. **Figure 3** compares the evolution of the carbon and nitrogen content for different fiber diameters after reaction times of 2 h and 24 h. After 24 h of reaction 1.45 wt% of carbon and 0.57 wt% of nitrogen were measured in the functionalized GM using elemental analysis. The percentages obtained were recalculated as 1.21 mmol/g for carbon and 0.41 mmol/g for nitrogen. These results are regarded as the maximum values of the degree of functionalization under these reaction conditions, and the silica used in this work. They serve as benchmark values for the evaluation of the functionalization extent of extruded fibers and monoliths. From reports on hydroxyl density, the hydroxyl content in silica thermal treated at 600 °C before functionalization is in the range of 1.0 to 2.5 #OH/nm^2 or 0.12 to 0.29 mmol OH/g.[39,43] Therefore, it can be concluded from the elemental analysis results that 1.4 to 3.4 amine groups are bonded for each hydroxyl on the surface.

Fibers, regardless of the diameter, show a decrease of ~15% in carbon and nitrogen content after 2 hours of reaction compared to the values of the GM sample (**Figure 3**). After 24 hours the fibers with diameters below 800 µm show similar carbon and nitrogen contents compared to those of GM. On the other hand, fibers with diameters larger than 800 µm still show ~10 % lower carbon and nitrogen content compared to those of GM. This is indicative of mass diffusion limitations occurring in the pore system of the fibers, leading to slower reaction kinetics. This can be explained by the narrow pore system of the fibers due to the dense particle packing inside the fibers and the absence of macropores, as measured by nitrogen sorption and mercury intrusion (**Figure S9** and **Figure S11**). One approach to overcome these diffusion limitations could be to further prolong the reaction time to reach less accessible pores. Consequently, to avoid diffusion limitations observed in the silanization of fibers, the 3D-printed structures were printed using 200 µm and 400 µm nozzles.

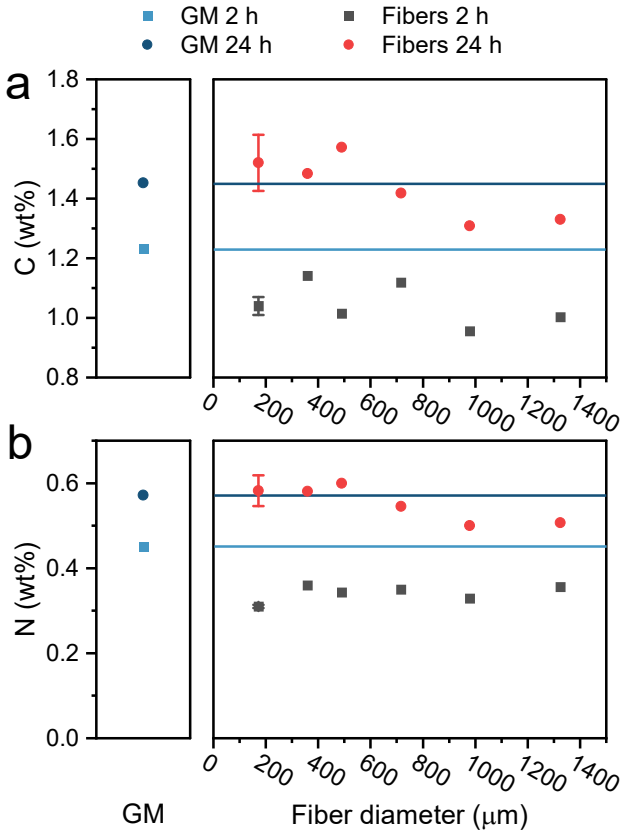

Figure 3. Concentration of carbon (**a.**) and nitrogen (**b**.), obtained by elemental analysis after silanization of GM and fibers of different diameters with 10 mM APTES solution in toluene and 3x excess triethylamine under reflux for 2 h and 24 h.

3.4. Functionalization of silica 3D-printed monoliths

Additionally to the diffusion within a fiber, homogeneous functionalization could be dependent of the internal configuration of the structure. Monoliths manufactured with different stackings, fiber diameters, and interfiber distances were reacted under controlled conditions using a batch reactor. These experiments were performed to explore if the configuration of the channels in the monolith could have a direct impact on the homogeneity of functional groups within the monolith. Different reaction conditions were evaluated to understand if possible diffusion limitations could be avoided by the silanization protocol.

3.4.1. Effect of the geometry

Carbon and nitrogen content of the functionalized samples 400/250-SC and 200/250-SC are lower than that of the functionalized GM as **Figure 4** shows, and no significant differences between the core and wall are observed. As the interfiber distance of the monolith decreases (200/150-SC and 200/150-FCC), differences in elemental composition between walls and core are observed, with twice as much carbon in the walls than in the cores. Therefore, the interfiber distance that drives the macro channeling inside the sample is a limiting factor in achieving a homogeneous functionalization using this protocol. Furthermore, the stacking design (SC or FCC) is not a determining factor for the homogeneity of functionalization. The results in **Figure 4** are conclusive on a threshold value of the IFD to obtain a homogenous coverage and intrusion of APTES using the silanization conditions. From these data, the threshold is between 150 µm and 250 µm.

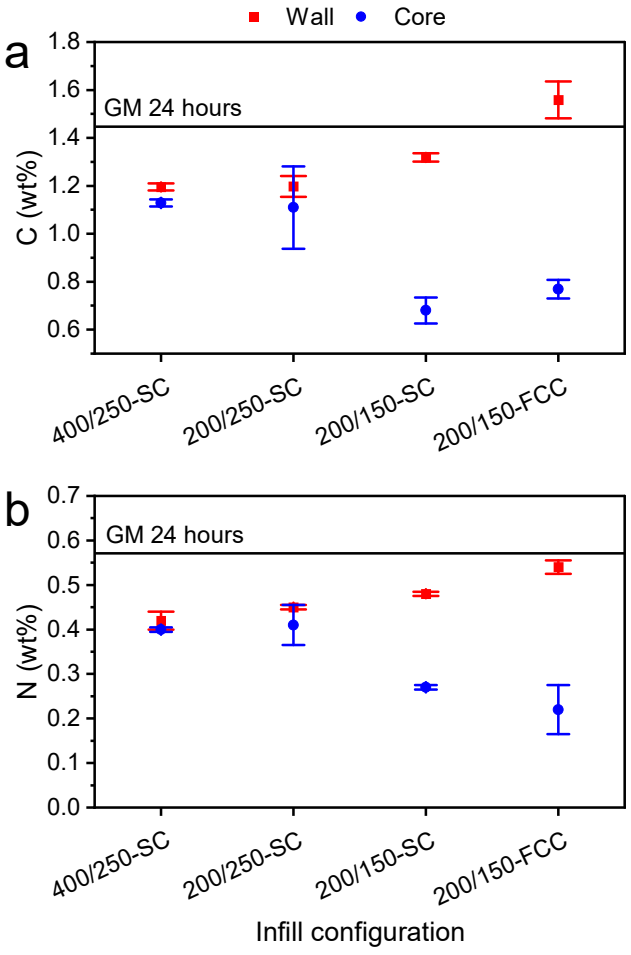

Figure 4. Percentage of carbon (**a**) and nitrogen (**b**) after silanization with APTES in toluene under reflux for 24 h as determined by elemental analysis of the monoliths 400/250-SC, 200/250-SC, 200/150-SC, and 200/150-FCC. The horizontal solid line represents the maximum functionalization reached in GM after 24 hours.

3.4.2. ζ-potential

The IEP and the shape of the ζ-potential curves are indicators for the extent of functionalization and homogeneity of the functional groups on the surface. From **Figure 5** it can be seen that the control sample did not reach a ζ-potential equal to zero. This is in agreement with previous evidence where silica suspensions below pH 3 become unstable due to dissolution and reorganization of the silica.[44] The functionalized core of sample 200/150-SC has an interpolated IEP of 4.3, while the highly functionalized wall has an interpolated IEP of 10.6. Typically, the IEP of silica treated with APTES is between 7.6 and 8.4.[34,45,46] It is possible that the presence of alumina on the surface of CLP contributes to a larger IEP.[47] The shape of the curve in **Figure 5** gives additional information about the chemical configuration of the surface.[48,49] A sharp transition between positive and negative ζ-potential values represents a highly homogeneous surface as seen for the walls of 200/150-SC and 400/250-SC, and the core of 400/250-SC. In addition, a gradual transition between positive and negative ζ-potential values typically represents a surface with different functionalities. This is the case of the core in sample 200/150-SC where the surface is composed of amine and hydroxyl groups due to the much lower degree of functionalization (**Figure 4**). Therefore, the results validate that the homogeneity of the functionalization is dependent of the interfiber distance in gap-spanning structures.

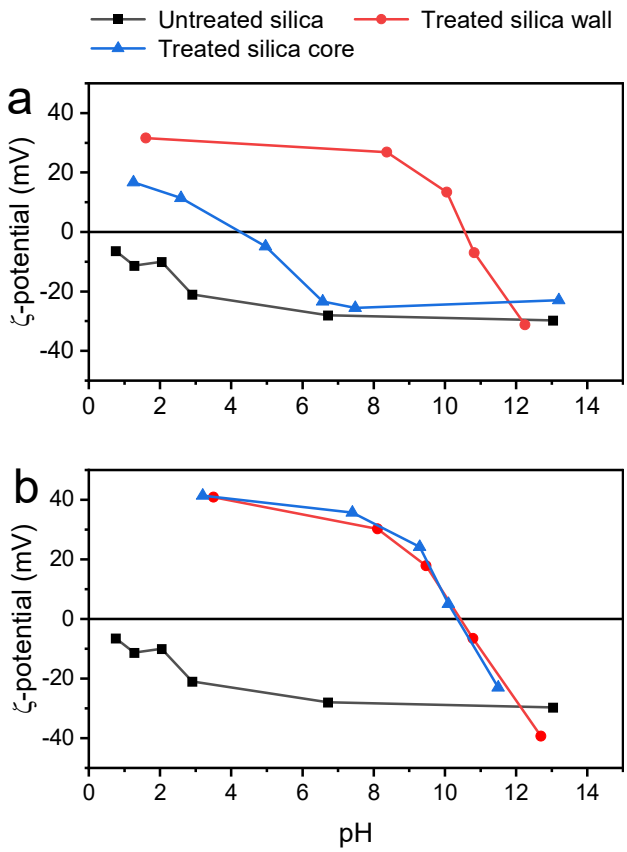

Figure 5. ζ-potential measurements at different pH values for determination of isoelectric points in 200/150-SC monolith (**a**), and 400/250-SC monolith (**b**). The lines are traced as reference and do not represent a model. The horizontal line in ζ-potential = 0 mV can be use as reference to visualize the isoelectric point in the graph.

3.4.3. Effect of the silanization conditions

Concentration, temperature, and time of reaction play a dominant role in the silanization.[36] A complete understanding of these parameters could lead to insights needed to obtain homogeneous coverage of the surface by the end of the synthetic procedure. Based on the results displayed in **Figure 6** the extent of the functionalization, as determined from the elemental composition, is dependent of the conditions of the silanization. The concentration of carbon and nitrogen for the walls of 400/250-SC and 200/150-SC structures is similar in each silanization treatment.

The concentration of APTES does have an effect in the extent of functionalization. From **Figure 6** the amount of carbon and nitrogen on the monoliths after the treatment 20-0.5-Ref, which has a theoretical excess of APTES related to the hydroxyls in the surface, is 30 % higher than the amount of carbon and nitrogen on the monoliths after the treatment 2.5-0.5-Ref, which has not enough APTES to fully functionalize the surface. Notably, the excess of APTES only has a small impact in the coverage of the surface. Therefore, it is recommended to use a slight excess of APTES for vacuum impregnation and further reaction. The extent of functionalization was similar for the samples 200/150-SC and 400/250-SC and no significant differences were observed between the extent of functionalization of the core and the walls in each sample. Therefore, under this conditions there is no effect of the concentration over the homogeneity of the reagent in the sample.

Different reaction temperatures do not have an effect for reactions performed for 0.5 h when APTES is used as limiting reagent as seen for the treatments 2.5-0.5-Ref and 2.5-0.5-RT in **Figure 6**, where the extent of functionalization is the same in the two treatments and no significant differences are identified in the percentage of carbon or nitrogen on the cores and on the walls. However, if an excess of APTES is used, the reflux of toluene in the treatment 20-0.5-Ref enhanced the surface coverage by 25% related with the reaction at room temperature using the treatment 20-0.5-RT. Therefore, refluxing is recommended for treatments performed for 0.5 h. On the other hand, when the reactions lasted 24 h, the extent of silanization was similar at different temperatures as observed for treatments 20-24-RT and 20-24-Ref in **Figure 6**. The treatments 20-24-RT and 20-24-Ref leaded to homogenous functionalization on the sample 400/250-SC. Contrary, the sample 200/150-SC has different content of carbon and nitrogen between the core and the walls showing the lack of homogeneity previously described in samples with interfiber distances of 150 µm.

The most critical silanization parameter to reach homogeneity between the core and the walls for 200/150-SC monoliths is therefore the reaction time. Treatment 20-24-Ref and 20-24-RT are directly related to non-homogeneity of amine groups in the monolith surface. However, the samples reacted with the treatments 2.5-0.5-Ref, 20-0.5-Ref, and 20-0.5-RT have similar contents of carbon and nitrogen on the cores and the walls. This similarity shows that for short reaction times, the reaction proceeds homogeneously throughout the sample, independent of the fiber diameter and interfiber distance. Furthermore, the homogeneity after 0.5 h is most likely attributed to an excellent wetting of the surface with the APTES solution achieved through vacuum impregnation. These results are comparable to the functionalization of GM and fibers with different diameters after 2 h of reaction time (**Figure 3**).

The reaction kinetics with 20 mM APTES solutions were carried out at room temperature and under reflux (**Figure S13**) considering that samples 200/150-SC were homogeneous after 0.5 h and non-homogeneous after 24 h. Consequently, it can be concluded from the kinetics plots that the extent of functionalization progress homogeneous through the sample the first 0.5 h, independent of the configuration, and over time, the diffusion of the reagent through the monolith channels plays a significant role in the final concentration of carbon and nitrogen in the walls and the core of the monolith. It is noteworthy that the maximum amount of carbon obtained in the walls of 200/150-SC, and in the core and walls of 400/250-SC, after treatment with 20-24-Ref and 20-24-RT is similar to that of the ESF and the GM experiments. Therefore, it can be concluded that the inhomogeneity in the samples after 24 hours is induced by diffusion limitations and lack of flow through interfiber channels of 150 μm. As a result, the APTES molecules are prevented from reaching the cores of the monoliths. These results, combined with the evaluation between geometries, infer that the interfiber distance for homogeneous functionalization is located between 150 μm and 250 μm.

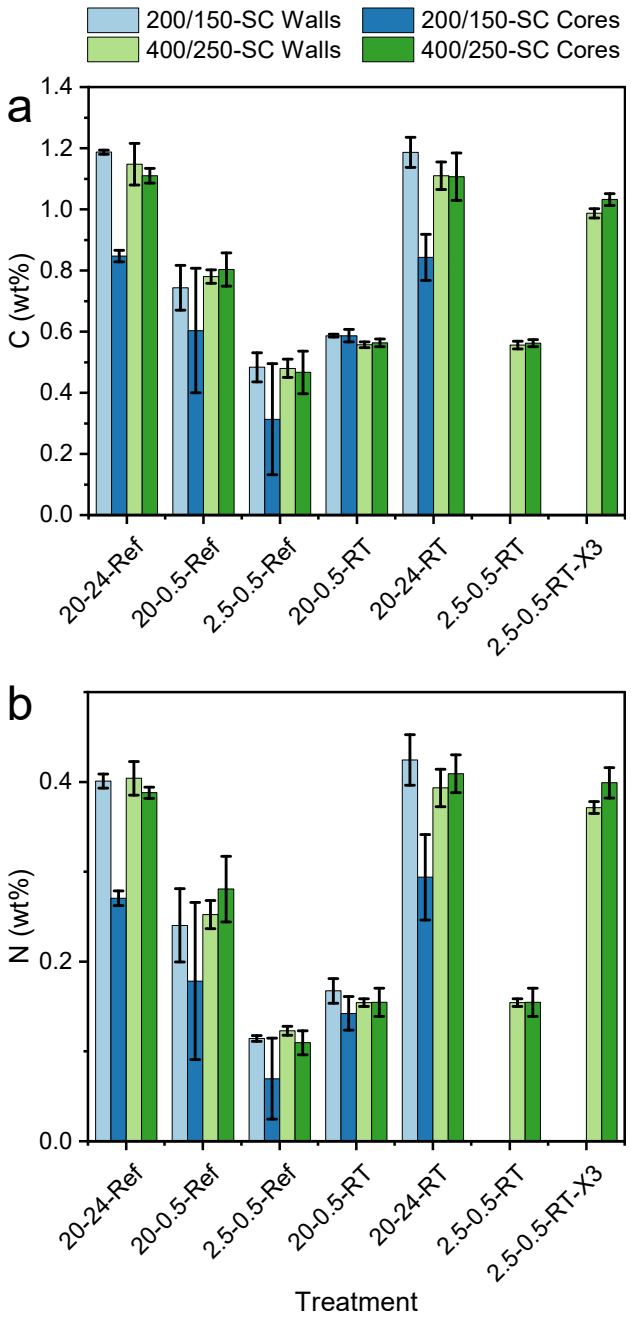

Figure 6. Elemental analysis results of functionalized silica monoliths under different APTES functionalization treatments. Weight percentage of carbon (**a**), and weight percentage of nitrogen (**b**).

3.4.4. Bonding of APTES to silica surfaces analyzed by ^{1}H-MAS, ^{13}C-CPMAS, and ^{29}Si-CPMAS NMR

The ^{1}H-MAS NMR spectrum of the control sample, shown in **Figure 7a**, has a single peak at δ = 4.8 ppm, this is assigned to silanol groups on the surface interacting with water as illustrated in **Figure S14a**.[50] The ^{1}H-MAS NMR spectra of the treated samples present additional peaks at δ = 0.4 ppm, δ = 1.1 ppm, and δ = 3.3 ppm assigned to the protons in the propylamine chain.[51–53] The assignments are illustrated in **Figure S14a**. After reaction with APTES, the silanol peak is shifted to the higher chemical shifts (downfield). The shifting of the peaks is more evident in the treatments 20-24-Ref where a higher density of propylamine groups was obtained. This shifting is a product of the interaction between silanol groups and protonated amines on the surface.[36,51] Moreover, The propylamine chains are far from each other at low concentrations and they have limited chances to interact with neighbor propylamine chains.[16] On the other hand, the sample reacted with the treatment 20-24-Ref has multiple peaks that can be associated to a second environment. Therefore, propylamine groups can be interacting among each other and with the silica surface leading to multiple environments for some of the protons.[36,37]

The ^{13}C-CPMAS NMR spectra of the control sample in **Figure 7b** does not show any peak as this does not have propylamine chains on the surface. Three main peaks were identified from the spectrum of the samples treated with APTES. **Figure S14** illustrates the carbon assignments in the propylamine chain. The peak at δ = 8.9 ppm corresponds to the carbon next to the silicium atom, the peak at δ = 21.4 ppm is assigned to the carbon in the middle of the chain, and the peak at δ = 41.8 ppm is for the carbon adjacent to the nitrogen atom.[54] Interestingly, a second peak near δ = 41.8 ppm is observed in the spectra of samples reacted for 0.5 h. This peak is indicative of a second environment like the one described from the ^{1}H-MAS NMR results. The

relative intensity of the ^{13}C-CPMAS NMR spectrum follows the order 20-24-Ref > 20-0.5-Ref > 20-0.5-RT > 2.5-0.5-Ref. The changes in the relative intensity of the peaks in **Figure 7b** are proportional to the percentages of carbon measured from the elemental analysis in **Figure 6**. Therefore, the signal enhancement is directly related with the abundance of functional groups bonded to the surface of the sample. Additionally, no peaks at δ = 18.4 ppm and δ = 58.4 ppm, associated with ethanol or with ethoxy groups from APTES, were identified in the ^{13}C-CPMAS NMR spectra.[35] This means that the APTES is condensed onto the surface thereby forming a covalent bond.

The ^{29}Si-CPMAS NMR spectra of the control sample in **Figure 7c** has Q^4, Q^3, and Q^2 silica groups at the surface assigned to the peaks in the spectrum located at δ = -112 ppm, δ = -101 ppm and δ = -90 ppm respectively.[51,53,55] The peak shoulder at δ = -90 ppm is more evident in the spectra of functionalized samples because Q^4 and Q^3 reacted with APTES before Q^2 silicas, which is to be expected as Q^2 silicas are known for being less reactive than Q^3.[56] Also, a new set of peaks in the functionalized samples is observed around δ = -60 ppm, this is assigned to T type silicon similar to the one illustrated in **Figure S14b**. The peaks located around the δ = -60 ppm region are conclusive concerning the formation of a covalent bond between APTES and the silica monolith surface.

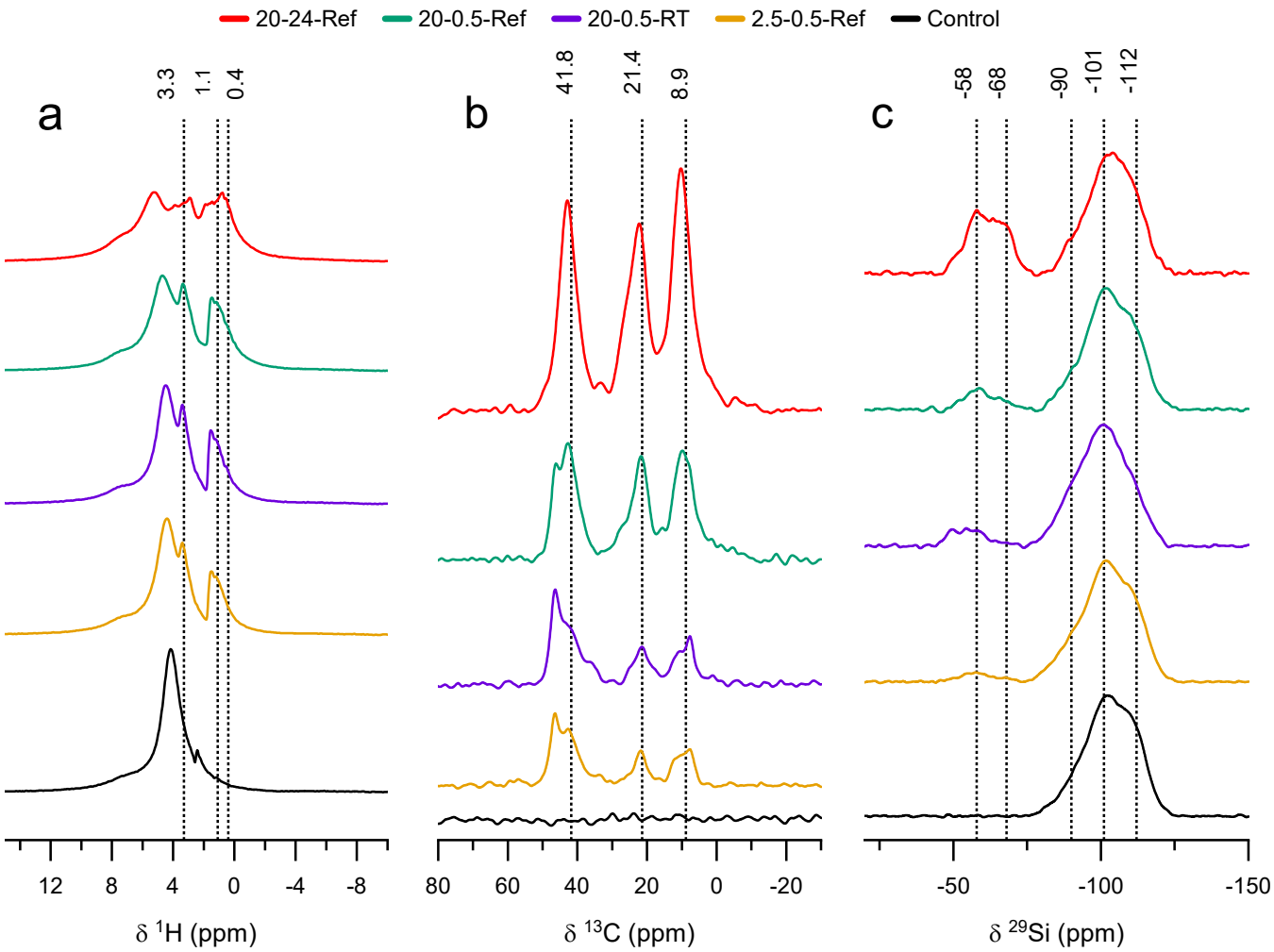

Figure 7. Solid state NMR spectra for silica 3D-printed monoliths functionalized with APTES, ^{1}H-MAS (**a**), ^{13}C-CPMAS (**b**), and ^{29}Si-CPMAS (**c**). Treatment name listed next to each spectrum.

3.5. Silanization after multiple vacuum wetting

Diffusion limitations within the fibers and the monolith resulted in inhomogeneities in samples 200/150-SC and long reaction times to reach similar carbon and nitrogen contents to those of the GM in the sample 400/250-SC as seen in **Figure S13a**. Silanization homogeneity was reached in the samples 200/150-SC and 400/250-SC with the treatment 20-0.5-RT. However, the extent of functionalization through the monolith was relatively low. In the second silanization procedure described in the methodology, the treatment 20-0.5-RT was repeated

three times using 400/250-SC structures to increase the extent of functionalization while assuring homogeneity. After these reaction cycles the carbon content was increased from 0.6 wt% to 1 wt% as seen in **Figure 6** for treatment 2.5-0.5-RT and 2.5-0.5-RT-X3 respectively. The 40% increase in carbon and nitrogen content, after three silanization cycles, allows a faster procedure to achieve a homogeneous distribution of the APTES, and a high concentration of APTES on the surface. In fact, 3 cycles of 0.5 h each yielded similar carbon and nitrogen density on the surface as the same reaction run for 17 h (**Figure S13**). This increase in the nitrogen and carbon content is attributed to the bonding of a first layer of APTES which could have a catalytic effect over the bonding of the fresh APTES added in the subsequent vacuum impregnation steps.[57] In addition, the hydrolysis in the washing step provides new hydroxyl groups that can be used for condensation of the fresh APTES added in the next vacuum impregnation cycle.[38]

3.6. Adsorption of palladium in functionalized fibers

Palladium adsorption is a well-known application for aminated surfaces, therefore this application was implemented to gather extra information about the availability of the bonded amines for Pd sorption.[58–60] The non-functionalized fibers show negligible adsorption capacities, Pd lower than 1 mg/g, in the pH range between 2 and 5 as seen in **Figure 8a**. The functionalized samples have adsorption capacities between 10 and 13 mg/g or 0.094 to 0.122 mmol/g. At pH 2 the Q_e of Pd was 20% lower than the same at pH 3, 4, and 5. Q_e for the evaluated silica is comparable with reported values in diverse materials and functional groups, especially with the previous reports using silica as support and 3-propylamine as functional moiety.[58,61] The result confirms the availability of the amine groups for sorption.

Clear differences are observed in the hydrolytic stability between the non-functionalized fibers, and the fibers functionalized with APTES. This was evaluated by measuring the silicium

concentration (mg/L) in the solutions after adsorption. **Figure 8b** shows the hydrolytic stability of the surface at different pH values. From the graph, silicium was detected in all the solutions after adsorption by the silica materials. The non-functionalized fibers have a significant degradation at pH 2 and pH 3 compared with the fibers functionalized with the treatment 20-24-Ref. A previous study demonstrated that at pH values below 3 the amine groups are protonated, and therefore the attacks over the surface do not occur extensively.[37] At pH 4 the content of silicium was similar for the functionalized and non-functionalized fibers. Finally, at pH 5 the non-functionalized samples perform better regarding silicium leaching compared to the functionalized fibers. Although the reasoning of this behavior is unknown, and at pH 5 the amines are still protonated, it is clear that propylamine groups on the surface of silica promote silica solubilization even at an acidic pH.[37]

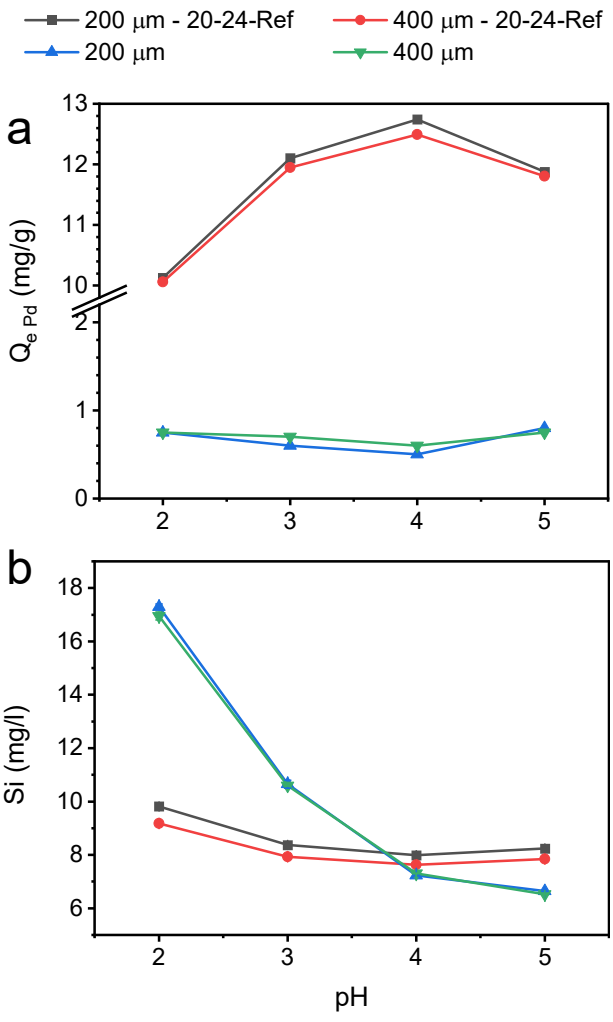

Figure 8. Impact of the pH on the adsorption capacity for Pd (mg/g) between pH 2 to 5 for fibers of 200 µm and 400 µm before and after the silanization with the treatment 20-24-Ref. (**a**) Residual Si concentration (mg/L) in solution (**b**), after stirring Pd solutions of 150 mg/L for 24 h with 200 mg of 200 µm and 400 µm fibers before and after functionalization with the treatment 20-24-Ref. The lines are for visual reference and do not represent a model.

4. Conclusion

The homogeneity of functional groups on the surface of 3D-printed porous silica structures was investigated after silanization in a batch reactor. The results demonstrate that APTES can be covalently bonded to the surface and homogenously distributed in 3D-printed silica monoliths with gap-spanning architectures that have interfiber distances greater than 250 µm. In addition, the extent of functionalization is dependent on fiber diameters above 359 µm and is independent of the configuration of the internal structure. Consequently, the reaction in vessels has high potential for applications where a large geometric surface area is not required, such as those with pressure drop limitations. However, challenges remain to achieve a homogeneous functionalization in structures with smaller interfiber distances. Alternative silanization protocols must be developed, aiming at the minimization of the mass diffusion limitations observed in the present study.

Multiple silanization cycles with vacuum impregnation and shorter reaction times yielded a higher extent of functionalization and a homogeneous distribution of the monoliths. The first layer of APTES is homogeneously distributed within the monolith. Subsequent reaction cycles allow the increase of the extent of functionalization as the first layer of bonded APTES has new hydroxyl groups which can be condensed with fresh APTES from the next silanization cycle enhancing the extent of functionalization while retaining the homogeneity of amine groups throughout the monolith.

This study is a baseline for functionalization of 3D-printed complex structures using batch reactors and demonstrates that fibers functionalized with propylamine groups are available for Pd adsorption. In addition, the concentration of amine groups in the reported structures is enough to achieve hydrolytic stability at pH values lower than 4. Further research aiming at the effective use of the monoliths in metal sorption or other applications will be focus on the increase of the specific surface area to allow a higher amount of functional groups and in the development of grafting protocols for higher geometric surface areas.

Supporting Information

Figure S11. Thermogravimetry measured in segmented samples before and after silanization with APTES

Figure S12. First derivative of the weight loss and mass spectroscopy for walls after treatment with 20-24-Ref

Figure S13. Kinetics of functionalization with APTES in SiO_2 monoliths

Figure S14. Solid state NMR assignments

Author Information

Corresponding Author: David Vogelsang*

*Email: david.vogelsang@vito.be

Notes

The authors declare no competing financial interest.

Acknowledgements

This work was partially supported by Hasselt University and the Research Foundation Flanders (FWO Vlaanderen; Hercules project AUHL/15/2-GOH3816N). We want to thank Dr. Jairo E. Perilla P. from the Universidad Nacional de Colombia for the discussions regarding the analysis of the rheology data. The authors gratefully acknowledge the technical assistance of A. De Wilde (TGA-MS, N_2 sorption, Hg intrusion), R. Kemps (SEM), J. De Wit (CHN analysis) and W. Brustens & K. Duyssens (ICP-AES).

References

(1) Goworek, J. Adsorption from Binary Solutions on Silanized Silica Gel. *Colloids and Surfaces*. 1990, pp 167–177. https://doi.org/10.1016/0166-6622(90)80070-k.

(2) Singla, B.; Krisdhasima, V.; McGuire, J. Adsorption Kinetics of Wild Type and Two Synthetic Stability Mutants of T4 Phage Lysozyme at Silanized Silica Surfaces. *J. Colloid Interface Sci.* **1996**, *182* (1), 292–296. https://doi.org/10.1006/jcis.1996.0463.

(3) Lepri, L.; Desideri, P. G.; Heimler, D. Thin-Layer Chromatography of Closely Related Polypeptides on Silanized Silica Gel. *Journal of Chromatography A*. 1981, pp 29–37. https://doi.org/10.1016/s0021-9673(00)81170-x.

(4) Buszewski, B.; Nondek, L.; Jurášek, A.; Berek, D. Preparation of Silanized Silica with High Ligand Density. The Effect of Silane Structure. *Chromatographia* **1987**, *23* (6), 442–446. https://doi.org/10.1007/BF02311822.

(5) Shin, K. S.; Cho, Y. K.; Choi, J.-Y.; Kim, K. Facile Synthesis of Silver-Deposited Silanized Magnetite Nanoparticles and Their Application for Catalytic Reduction of Nitrophenols. *Appl. Catal. A* **2012**, *413–414*, 170–175. https://doi.org/10.1016/j.apcata.2011.11.006.

(6) Li, H.-L.; Perkas, N.; Li, Q.-L.; Gofer, Y.; Koltypin, Y.; Gedanken, A. Improved Silanization Modification of a Silica Surface and Its Application to the Preparation of a Silica-Supported Polyoxometalate Catalyst. *Langmuir* **2003**, *19* (24), 10409–10413. https://doi.org/10.1021/la035280l.

(7) Yokoi, T.; Kubota, Y.; Tatsumi, T. Amino-Functionalized Mesoporous Silica as Base Catalyst and Adsorbent. *Appl. Catal. A* **2012**, *421–422*, 14–37. https://doi.org/10.1016/j.apcata.2012.02.004.

(8) Crudden, C. M.; Sateesh, M.; Lewis, R. Mercaptopropyl-Modified Mesoporous Silica: A Remarkable Support for the Preparation of a Reusable, Heterogeneous Palladium Catalyst for Coupling Reactions. *J. Am. Chem. Soc.* **2005**, *127* (28), 10045–10050. https://doi.org/10.1021/ja0430954.

(9) Mureseanu, M.; Cioatera, N.; Trandafir, I.; Georgescu, I.; Fajula, F.; Galarneau, A. Selective Cu2+ Adsorption and Recovery from Contaminated Water Using Mesoporous Hybrid Silica Bio-Adsorbents. *Microporous Mesoporous Mater.* **2011**, *146* (1), 141–150. https://doi.org/10.1016/j.micromeso.2011.04.026.

(10) Mosai, A. K.; Chimuka, L.; Cukrowska, E. M.; Kotzé, I. A.; Tutu, H. Batch and Flow-through Column Adsorption Study: Recovery of Pt4+ from Aqueous Solutions by 3-Aminopropyl(Diethoxy)Methylsilane Functionalised Zeolite (APDEMSFZ). *Environ. Dev. Sustainability* **2021**, *23* (5), 7041–7062. https://doi.org/10.1007/s10668-020-00903-x.

(11) Yadav, A. R.; Sriram, R.; Carter, J. A.; Miller, B. L. Comparative Study of Solution-Phase and Vapor-Phase Deposition of Aminosilanes on Silicon Dioxide Surfaces. *Mater. Sci. Eng. C Mater. Biol. Appl.* **2014**, *35*, 283–290. https://doi.org/10.1016/j.msec.2013.11.017.

(12) Forzano, A. V.; Cain, C. N.; Rutan, S. C.; Collinson, M. M. In Situ Silanization for Continuous Stationary Phase Gradients on Particle Packed LC Columns. *Anal. Methods* **2019**, *11* (29), 3648–3656. https://doi.org/10.1039/C9AY00960D.

(13) Sunny, S.; Vogel, N.; Howell, C.; Vu, T. L.; Aizenberg, J. Lubricant-infused Nanoparticulate Coatings Assembled by Layer-by-layer Deposition. *Adv. Funct. Mater.* **2014**, *24* (42), 6658–6667. https://doi.org/10.1002/adfm.201401289.

(14) Girimonte, R.; Testa, F.; Turano, M.; Leone, G.; Gallo, M.; Golemme, G. Amine-Functionalized Mesoporous Silica Adsorbent for CO2 Capture in Confined-Fluidized Bed: Study of the Breakthrough Adsorption Curves as a Function of Several Operating Variables. *Processes* **2022**, *10* (2), 422. https://doi.org/10.3390/pr10020422.

(15) Qiao, B.; Wang, T.-J.; Gao, H.; Jin, Y. High Density Silanization of Nano-Silica Particles Using γ-Aminopropyltriethoxysilane (APTES). *Appl. Surf. Sci.* **2015**, *351*, 646–654. https://doi.org/10.1016/j.apsusc.2015.05.174.

(16) Paul, G.; Musso, G. E.; Bottinelli, E.; Cossi, M.; Marchese, L.; Berlier, G. Investigating the Interaction of Water Vapour with Aminopropyl Groups on the Surface of Mesoporous Silica Nanoparticles. *Chemphyschem* **2017**, *18* (7), 839–849. https://doi.org/10.1002/cphc.201601135.

(17) Thakkar, H.; Eastman, S.; Al-Mamoori, A.; Hajari, A.; Rownaghi, A. A.; Rezaei, F. Formulation of Aminosilica Adsorbents into 3D-Printed Monoliths and Evaluation of Their CO2 Capture Performance. *ACS Appl. Mater. Interfaces* **2017**, *9* (8), 7489–7498. https://doi.org/10.1021/acsami.6b16732.

(18) Laaniste, A.; Marechal, A.; El-Debs, R.; Randon, J.; Dugas, V.; Demesmay, C. "Thiol-Ene" Photoclick Chemistry as a Rapid and Localizable Functionalization Pathway for Silica Capillary Monolithic Columns. *J. Chromatogr. A* **2014**, *1355*, 296–300. https://doi.org/10.1016/j.chroma.2014.06.031.

(19) Allen, D.; El Rassi, Z. Capillary Electrochromatography with Monolithic Silica Column: I. Preparation of Silica Monoliths Having Surface-bound Octadecyl Moieties and Their Chromatographic Characterization and Applications to the Separation of Neutral and Charged Species. *Electrophoresis* **2003**, *24* (3), 408–420. https://doi.org/10.1002/elps.200390051.

(20) Ma, Y.; Hao, L.; Lin, X.; Liu, X.; Qiu, X.; Zhang, X.; Hu, X. An In-Tube Aptamer/Gold Nanoparticles Coated Capillary Solid-Phase Microextraction for Separation of Adenosine in Serum and Urine Samples. *J. Chromatogr. A* **2020**, *1611*, 460617. https://doi.org/10.1016/j.chroma.2019.460617.

(21) Li, M.; Shen, H.; Zhou, Z.; He, W.; Su, P.; Song, J.; Yang, Y. Controllable and High-performance Immobilized Enzyme Reactor: DNA-directed Immobilization of Multienzyme in Polyamidoamine Dendrimer-functionalized Capillaries. *Electrophoresis* **2020**, *41* (5–6), 335–344. https://doi.org/10.1002/elps.201900428.

(22) Xu, M.; Feng, Y.; Li, Z.; Wang, X.; Li, C.; Jiang, H.; Chen, Y. A Novel, Efficient and Cost-Effective Synthesis Technique for the Development of Superhydrophobic Glass Surface. *J. Alloys Compd.* **2019**, *781*, 1175–1181. https://doi.org/10.1016/j.jallcom.2018.12.084.

(23) AlSuhaimi, A. O.; AlMohaimadi, K. M.; AlAlawi, B. N.; Ali, I. A Novel Porous Silica Monolith Functionalized with 5-Amino-1,10-Phenanthroline for SPE of Metal Ions in Groundwater Samples Prior to Their Analysis Using ICP-MS. *Anal. Methods* **2018**, *10* (20), 2337–2346. https://doi.org/10.1039/C8AY00442K.

(24) Courtois, J.; Szumski, M.; Byström, E.; Iwasiewicz, A.; Shchukarev, A.; Irgum, K. A Study of Surface Modification and Anchoring Techniques Used in the Preparation of

Monolithic Microcolumns in Fused Silica Capillaries. *J. Sep. Sci.* **2006**, *29* (1), 14–24. https://doi.org/10.1002/jssc.200500294.

(25) Li, Z.; Sellaoui, L.; Gueddida, S.; Dotto, G. L.; Ben Lamine, A.; Bonilla-Petriciolet, A.; Badawi, M. Adsorption of Methylene Blue on Silica Nanoparticles: Modelling Analysis of the Adsorption Mechanism via a Double Layer Model. *J. Mol. Liq.* **2020**, *319*, 114348. https://doi.org/10.1016/j.molliq.2020.114348.

(26) Smay, J. E.; Gratson, G. M.; Shepherd, R. F.; Cesarano, J.; Lewis, J. A. Directed Colloidal Assembly of 3D Periodic Structures. *Adv. Mater.* **2002**, *14* (18), 1279–1283. 3.0.co;2-a">https://doi.org/10.1002/1521-4095(20020916)14:18<1279::aid-adma1279>3.0.co;2-a.

(27) Elsayed, H.; Colombo, P.; Bernardo, E. Direct Ink Writing of Wollastonite-Diopside Glass-Ceramic Scaffolds from a Silicone Resin and Engineered Fillers. *J. Eur. Ceram. Soc.* **2017**, *37* (13), 4187–4195. https://doi.org/10.1016/j.jeurceramsoc.2017.05.021.

(28) Nommeots-Nomm, A.; Lee, P. D.; Jones, J. R. Direct Ink Writing of Highly Bioactive Glasses. *J. Eur. Ceram. Soc.* **2018**, *38* (3), 837–844. https://doi.org/10.1016/j.jeurceramsoc.2017.08.006.

(29) Destino, J. F.; Dudukovic, N. A.; Johnson, M. A.; Nguyen, D. T.; Yee, T. D.; Egan, G. C.; Sawvel, A. M.; Steele, W. A.; Baumann, T. F.; Duoss, E. B.; Suratwala, T.; Dylla-Spears, R. 3D Printed Optical Quality Silica and Silica–Titania Glasses from Sol–Gel Feedstocks. *Adv. Mater. Technol.* **2018**, *3* (6), 1700323. https://doi.org/10.1002/admt.201700323.

(30) Zhao, S.; Siqueira, G.; Drdova, S.; Norris, D.; Ubert, C.; Bonnin, A.; Galmarini, S.; Ganobjak, M.; Pan, Z.; Brunner, S.; Nyström, G.; Wang, J.; Koebel, M. M.; Malfait, W. J.

Additive Manufacturing of Silica Aerogels. *Nature* **2020**, *584* (7821), 387–392. https://doi.org/10.1038/s41586-020-2594-0.

(31) Guo, Z.; Yang, R.; Wang, T.; An, L.; Ren, S.; Zhou, C. Cost-Effective Additive Manufacturing of Ambient Pressure-Dried Silica Aerogel. *J. Manuf. Sci. Eng.* **2020**, *143* (1). https://doi.org/10.1115/1.4048740.

(32) Putz, F.; Scherer, S.; Ober, M.; Morak, R.; Paris, O.; Hüsing, N. 3D Printing of Hierarchical Porous Silica and α-Quartz. *Adv. Mater. Technol.* **2018**, *3* (7), 1800060. https://doi.org/10.1002/admt.201800060.

(33) Ferrizz, R. M.; Stuecker, J. N.; Cesarano, J.; Miller, J. E. Monolithic Supports with Unique Geometries and Enhanced Mass Transfer. *Ind. Eng. Chem. Res.* **2005**, *44* (2), 302–308. https://doi.org/10.1021/ie049468r.

(34) Goscianska, J.; Olejnik, A.; Nowak, I. APTES-Functionalized Mesoporous Silica as a Vehicle for Antipyrine – Adsorption and Release Studies. *Colloids Surf. A Physicochem. Eng. Asp.* **2017**, *533*, 187–196. https://doi.org/10.1016/j.colsurfa.2017.07.043.

(35) Tonlé, I. K.; Diaco, T.; Ngameni, E.; Detellier, C. Nanohybrid Kaolinite-Based Materials Obtained from the Interlayer Grafting of 3-Aminopropyltriethoxysilane and Their Potential Use as Electrochemical Sensors. *Chem. Mater.* **2007**, *19* (26), 6629–6636. https://doi.org/10.1021/cm702206z.

(36) Zhu, M.; Lerum, M. Z.; Chen, W. How to Prepare Reproducible, Homogeneous, and Hydrolytically Stable Aminosilane-Derived Layers on Silica. *Langmuir* **2012**, *28* (1), 416–423. https://doi.org/10.1021/la203638g.

(37) Etienne, M.; Walcarius, A. Analytical Investigation of the Chemical Reactivity and Stability of Aminopropyl-Grafted Silica in Aqueous Medium. *Talanta* **2003**, *59* (6), 1173–1188. https://doi.org/10.1016/S0039-9140(03)00024-9.

(38) Krasnoslobodtsev, A. V.; Smirnov, S. N. Effect of Water on Silanization of Silica by Trimethoxysilanes. *Langmuir* **2002**, *18* (8), 3181–3184. https://doi.org/10.1021/la015628h.

(39) Mueller, R.; Kammler, H. K.; Wegner, K.; Pratsinis, S. E. OH Surface Density of SiO2 and TiO2 by Thermogravimetric Analysis. *Langmuir* **2003**, *19* (1), 160–165. https://doi.org/10.1021/la025785w.

(40) Dudukovic, N. A.; Wong, L. L.; Nguyen, D. T.; Destino, J. F.; Yee, T. D.; Ryerson, F. J.; Suratwala, T.; Duoss, E. B.; Dylla-Spears, R. Predicting Nanoparticle Suspension Viscoelasticity for Multimaterial 3D Printing of Silica–Titania Glass. *ACS Appl. Nano Mater.* **2018**, *1* (8), 4038–4044. https://doi.org/10.1021/acsanm.8b00821.

(41) Feilden, E. Additive Manufacturing of Ceramics and Ceramic Composites via Robocasting, Imperial College London, 2017. https://doi.org/10.25560/55940.

(42) del-Mazo-Barbara, L.; Ginebra, M.-P. Rheological Characterisation of Ceramic Inks for 3D Direct Ink Writing: A Review. *J. Eur. Ceram. Soc.* **2021**, *41* (16), 18–33. https://doi.org/10.1016/j.jeurceramsoc.2021.08.031.

(43) Sneh, O.; George, S. M. Thermal Stability of Hydroxyl Groups on a Well-Defined Silica Surface. *J. Phys. Chem.* **1995**, *99* (13), 4639–4647. https://doi.org/10.1021/j100013a039.

(44) Antonio Alves Júnior, J.; Baptista Baldo, J. The Behavior of Zeta Potential of Silica Suspensions. *New J. Glas. Ceram.* **2014**, *04* (02), 29–37. https://doi.org/10.4236/njgc.2014.42004.

(45) Nikolić, M. P.; Giannakopoulos, K. P.; Bokorov, M.; Srdić, V. V. Effect of Surface Functionalization on Synthesis of Mesoporous Silica Core/Shell Particles. *Microporous Mesoporous Mater.* **2012**, *155*, 8–13. https://doi.org/10.1016/j.micromeso.2011.12.046.

(46) Koopal, L. K.; Yang, Y.; Minnaard, A. J.; Theunissen, P. L. M.; Van Riemsdijk, W. H. Chemical Immobilisation of Humic Acid on Silica. *Colloids Surf. A Physicochem. Eng. Asp.* **1998**, *141* (3), 385–395. https://doi.org/10.1016/S0927-7757(97)00170-2.

(47) Eskandarloo, H.; Arshadi, M.; Enayati, M.; Abbaspourrad, A. Highly Efficient Recovery of Heparin Using a Green and Low-Cost Quaternary Ammonium Functionalized Halloysite Nanotube. *ACS Sustainable Chem. Eng.* **2018**, *6* (11), 15349–15360. https://doi.org/10.1021/acssuschemeng.8b03793.

(48) Goller, M. I.; Barthet, C.; McCarthy, G. P.; Corradi, R.; Newby, B. P.; Wilson, S. A.; Armes, S. P.; Luk, S. Y. Synthesis and Characterization of Surface-Aminated Polypyrrole–Silica Nanocomposites. *Colloid Polym. Sci.* **1998**, *276* (11), 1010–1018. https://doi.org/10.1007/s003960050340.

(49) Wu, Z.; Xiang, H.; Kim, T.; Chun, M.-S.; Lee, K. Surface Properties of Submicrometer Silica Spheres Modified with Aminopropyltriethoxysilane and Phenyltriethoxysilane. *J. Colloid Interface Sci.* **2006**, *304* (1), 119–124. https://doi.org/10.1016/j.jcis.2006.08.055.

(50) Hartmeyer, G.; Marichal, C.; Lebeau, B.; Rigolet, S.; Caullet, P.; Hernandez, J. Speciation of Silanol Groups in Precipitated Silica Nanoparticles by 1H MAS NMR Spectroscopy. *J. Phys. Chem. C Nanomater. Interfaces* **2007**, *111* (26), 9066–9071. https://doi.org/10.1021/jp071490l.

(51) Kim, S.-H.; Han, O.-H.; Kim, J.-K.; Lee, K.-H. Multinuclear Solid-State NMR Investigation of Nanoporous Silica Prepared by Sol-Gel Polymerization Using Sodium

Silicate. *Bull. Korean Chem. Soc.* **2011**, *32* (10), 3644–3649. https://doi.org/10.5012/bkcs.2011.32.10.3644.

(52) Lee, H.; Sung, D.; Kim, J.; Kim, B.-T.; Wang, T.; An, S. S. A.; Seo, S.-W.; Yi, D. K. Silica Nanoparticle-Based Dual Imaging Colloidal Hybrids: Cancer Cell Imaging and Biodistribution. *Int. J. Nanomedicine* **2015**, *10 Spec Iss*, 215–225. https://doi.org/10.2147/IJN.S88311.

(53) Crucho, C. I. C.; Baleizão, C.; Farinha, J. P. S. Functional Group Coverage and Conversion Quantification in Nanostructured Silica by 1H NMR. *Anal. Chem.* **2017**, *89* (1), 681–687. https://doi.org/10.1021/acs.analchem.6b03117.

(54) Mugica, L. C.; Rodríguez-Molina, B.; Ramos, S.; Kozina, A. Surface Functionalization of Silica Particles for Their Efficient Fluorescence and Stereo Selective Modification. *Colloids Surf. A Physicochem. Eng. Asp.* **2016**, *500*, 79–87. https://doi.org/10.1016/j.colsurfa.2016.04.002.

(55) Protsak, I. S.; Morozov, Y. M.; Dong, W.; Le, Z.; Zhang, D.; Henderson, I. M. A 29Si, 1H, and 13C Solid-State NMR Study on the Surface Species of Various Depolymerized Organosiloxanes at Silica Surface. *Nanoscale Res. Lett.* **2019**, *14* (1), 160. https://doi.org/10.1186/s11671-019-2982-2.

(56) Hair, M. L. Hydroxyl Groups on Silica Surface. *J. Non-Cryst. Solids* **1975**, *19*, 299–309. https://doi.org/10.1016/0022-3093(75)90095-2.

(57) Kaas, R. L.; Kardos, J. L. The Interaction of Alkoxy Silane Coupling Agents with Silica Surfaces. *Polym. Eng. Sci.* **1971**, *11* (1), 11–18. https://doi.org/10.1002/pen.760110104.

(58) Dobrzyńska, J.; Dobrowolski, R.; Olchowski, R.; Zięba, E.; Barczak, M. Palladium Adsorption and Preconcentration onto Thiol- and Amine-Functionalized Mesoporous Silicas with Respect to Analytical Applications. *Microporous Mesoporous Mater.* **2019**, *274*, 127–137. https://doi.org/10.1016/j.micromeso.2018.07.038.

(59) Li, M.; Tang, S.; Feng, J.; Huang, K.; Meng, X.; Gao, F.; Jiang, S. Highly Efficient Separation/Recycling Palladium(II) Ions from Aqueous Solutions by Silica Gel-Coated Graphene Oxide Modified with Mercapto Groups. *Metall. Mater. Trans. B* **2019**, *50* (6), 2747–2757. https://doi.org/10.1007/s11663-019-01697-8.

(60) Tong, A.; Akama, Y.; Tanaka, S. Selective Preconcentration of Au(III), Pt(IV) and Pd(II) on Silica Gel Modified with γ-Aminopropyltriethoxysilane. *Anal. Chim. Acta* **1990**, *230*, 179–181. https://doi.org/10.1016/S0003-2670(00)82778-6.

(61) Sivrikaya, S.; Altundag, H.; Zengin, M.; Imamoglu, M. Separation, Preconcentration, and Recovery of Pd(II) Ions Using Newly Modified Silica Gel with Bis(3-Aminopropyl)Amine. *Sep. Sci. Technol.* **2011**, *46* (13), 2032–2040. https://doi.org/10.1080/01496395.2011.572111.

Graphical abstract

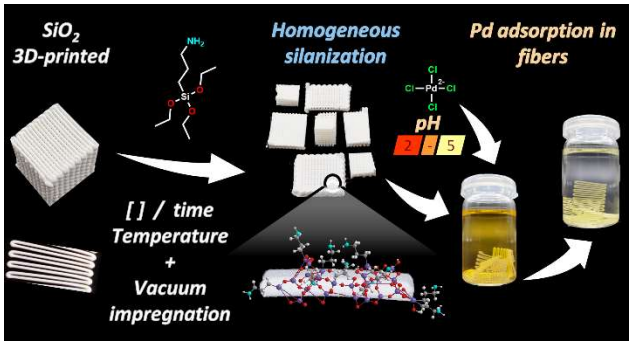

Caption: Homogeneity and extent of silanization on 3D-printed silica structures were evaluated using 3-aminopropyltriethoxysilane. The extent of functionalization does not have differences for fibers below 400 µm. Vacuum impregnation and short reaction times provide homogeneously functionalized structures. The extent of functionalization was increased by doing multiple cycles. On the other hand, a single cycle leads to inhomogeneous functionalization for structures with interfiber distances below 250 µm. Functionalized fibers were effective adsorbing palladium in acid solutions. In addition, the functionalized material showed neglectable solubility its low pH values.

1

2